Symmetric and standard matter neutrino resonances above merging compact objects

A. Malkus,[1,*] G. C. McLaughlin,[1,†] and R. Surman[2,‡]

[1]*Department of Physics, North Carolina State University, Raleigh, North Carolina 27695, USA*
[2]*Department of Physics, University of Notre Dame, Notre Dame, Indiana 46656, USA*

Matter neutrino resonances (MNRs) can occur in environments where the flux of electron antineutrinos is greater than the flux of electron neutrinos. These resonances may result in dramatic neutrino flavor transformation. Compact object merger disks are an example of an environment where electron antineutrinos outnumber neutrinos. We study MNR resonances in several such disk configurations and find two qualitatively different types of matter-neutrino resonances: a standard MNR and a symmetric MNR. We examine the transformation that occurs in each type of resonance and explore the consequences for nucleosynthesis.

I. INTRODUCTION

Neutrinos shape the physical phenomena surrounding compact object mergers, from the dynamics of the disk or a hypermassive-neutron star itself [1–4], to the energetic jets, e.g., [5] that may form them. Neutrinos also play an important role in the nucleosynthesis that takes place in and around disks [6–9]. For example, the wind outflows [10,11] above disks can be home to nucleosynthesis, including perhaps the r process, depending on neutrino flavor composition [2,9,12–16]. The neutrino flavor composition above the neutrino trapping surface depends not only on thermodynamics in the trapped regions but also the oscillation of neutrinos as they leave the disk. The high neutrino density coupled with high matter density provides an environment where several kinds of oscillation may take place. Neutrinos emitted from mergers can undergo the same types of transformations that neutrinos from supernovae do [17], as well as oscillations not previously seen elsewhere (except for in collapsars [18]), called matter neutrino resonance (MNR) transitions [19]. The MNR takes place when the matter potential and the neutrino self-interaction potential are the same size and have opposite signs.

Much of the previous work on neutrino transformation in high neutrino density environments has considered matter and self-interaction potentials of the same sign. For example, for the case of core collapse supernovae neutrinos, it has been pointed out that several types of transformations can occur in such systems which have a slight electron neutrino excess, start at high neutrino density, and end at low neutrino density; for recent work see e.g. Refs. [20–27]. At very high densities of neutrinos, more than one type of synchronized neutrino oscillation can occur, e.g. Refs. [28–30]. At very low densities of neutrinos, the neutrino self-interaction potential is unimportant, and Mikheyev-Smirnov-Wolfenstein (MSW) oscillations can take place when the scale of the matter potential is the same as the vacuum scale. In between these extreme regimes of synchronized and MSW oscillations, large scale flavor transformation can take place when the neutrino self-interaction potential approaches the vacuum oscillation scale [31,32] and the neutrinos and antineutrinos enter the transition region nearly in flavor eigenstates, e.g. Refs. [31–39]. During the transition, the neutrinos and antineutrinos are said to be "locked" as their survival probabilities mirror each other and the phenomenon is referred to as "bipolar" or "nutation" oscillation.

Unique to settings where the neutrino interaction potential and the matter potential have opposite signs, another oscillation phenomenon can be possible [18,19]. In Ref. [18] it was shown that collapsar-type disks may be home to MNRs and that the MNR may result in flavor transformation that alters nucleosynthesis. The understanding of the MNR was expanded in Ref. [19], where the standard MNR was explored in detail. A MNR begins when the scale of the matter potential and the neutrino self-interaction potential are the same and can cancel. A MNR transition can cause a dramatic change in the flavor of neutrinos. During the transformation, the neutrino self-interaction potential matches the size of the matter potential over an extended period of time. The transition continues as long as the neutrinos can change flavor in such a way that the potential matching is possible. Once the neutrinos can no longer keep up with the matter potential, then the transformation ceases.

Whether a MNR region occurs and whether it results in flavor transformation depends upon the configuration of the emission surfaces. We examine two qualitatively different types of self-interaction potentials that can arise from mergers. We point out that, while there exist two different

*acmalkus@ncsu.edu
†gcmclaug@ncsu.edu
‡rsurman@nd.edu

045021-1

self-interaction potentials, which result in distinct outcomes, the oscillation phenomena are both well described as MNR transitions. Our study is presented in this paper as follows. First we discuss representative disk configurations in Sec. II, and then we discuss oscillation calculations in Sec. III. We present neutrino oscillation calculation results in Sec. IV and the results of nucleosynthesis calculations in Sec. V. We then conclude in Sec. VI.

II. ACCRETION DISK CONFIGURATIONS

Similar to core collapse supernovae, the mergers of compact objects like two neutron stars or a black hole and a neutron star release vast amounts of energy in the form of neutrinos and antineutrinos. However, unlike supernovae, these systems begin with a composition of almost entirely neutrons. After the collision, the material is heated, and the electron fraction increases. As a consequence, the resulting emission of antineutrinos is greater than the emission of neutrinos. Electron neutrinos and antineutrinos are thought to dominate the flux [1–3,11,40], and other flavors may not be trapped at all [41]. Simulations of compact object mergers show small amounts of mu and tau neutrinos with a luminosity of up to 1.5×10^{52} erg/s [1]. This luminosity is about 1/10th of the luminosity of electron antineutrinos.

Guided by these results, we generate a set of representative disk models and calculate the neutrino oscillation pattern above them. The disk models used in the following calculations are inspired by those in Refs. [13,42–44], for a merger of a $2.5 M_\odot$ black hole and a $1.6 M_\odot$ neutron star that forms a black hole with mass $3.85 M_\odot$ and spin parameter $a = 0.6$. For ease of calculation, the disks are taken to be geometrically thin. We use two general types of models: one with all three types of neutrino emission coming from a disk with a single maximum radius and a second where each of the three types comes from a unique disk with its own radius.

Each of the three kinds of neutrinos (electron neutrinos, electron antineutrinos, and all other flavors of neutrinos and antineutrinos) are taken to have different temperatures. These temperatures and radii are listed in Table I for our single radius model and Table II for our multiple radius

TABLE I. Single radius model: Parameters for neutrino emission from a single surface. Fluxes are taken to be thermal Fermi Dirac fluxes for the electron neutrino and electron antineutrinos. For mu and tau flavor neutrinos and antineutrinos, the flux is taken to be the thermal flux rescaled by an overall parameter specified in each example.

a	T_a (MeV)	R_a (cm)
ν_e	6.4	4.5×10^6
$\nu_{\mu,\tau}$	7.4	4.5×10^6
$\bar{\nu}_e$	7.1	4.5×10^6
$\bar{\nu}_{\mu,\tau}$	7.4	4.5×10^6

TABLE II. Multiple radius model: Parameters for neutrino emission from several surfaces. Fluxes are taken to be thermal Fermi Dirac fluxes for the electron neutrino and electron antineutrinos. For mu and tau flavor neutrinos, the fluxes are taken to be the thermal fluxes as well, but the radius of the emission is taken to be different as specified in each example.

a	T_a (MeV)	R_a (cm)
ν_e	5.9	5.2×10^6
$\nu_{\mu,\tau}$	9.9	variable
$\bar{\nu}_e$	7.8	3.9×10^6
$\bar{\nu}_{\mu,\tau}$	9.9	variable

model. We further vary the amount of ν_μ, ν_τ, $\bar{\nu}_\mu$, and $\bar{\nu}_\tau$ within each type of model.

We follow a test neutrino as it leaves each disk model at 45° from the plane of the disk. The test neutrino starts above the disk and follows a radial trajectory outward, which we show in Fig. 1. The trajectory follows the mass outflow as it leaves from the disk. We use a parametrized outflow velocity, u, as in Ref. [45]. The velocity depends on the acceleration of the material, β, and the eventual velocity of the material at infinity, v_∞,

$$|u| = v_\infty \left(1 - \frac{R_{\text{inner}}}{R}\right)^\beta, \tag{1}$$

where R is the distance from the center of the disk and R_{inner} is the initial position of the material, which we take to be $R_{\text{inner}} = 2.0 \times 10^6$ cm. As the neutrino travels along the trajectory, the neutrino will feel potentials based on its position. The matter potential, due to coherent forward scattering with electrons and positrons, is computed from the number density based on the outflow model, which assumes a constant mass outflow rate. The outflow model, with $s/k = 50$, $\beta = 2.0$, and $v_\infty = 0.1c$, yields net electron number density, $N_e(t)$, where t parametrizes the position along the trajectory. The position $t = 0$ is the start of the trajectory.
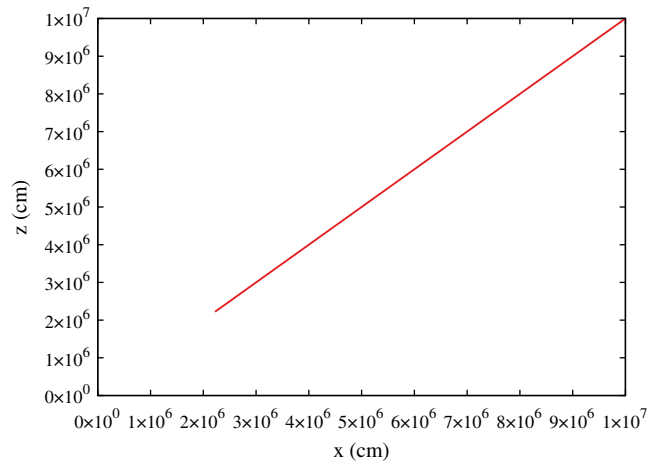

FIG. 1. Trajectory of the test neutrino, $\vec{r} = (x, y = 0, z)$.

III. CALCULATIONS

We calculate the flavor transformation of neutrinos and antineutrinos as they travel along the trajectory which we show in Fig. 1. The evolution of neutrinos and antineutrinos is computed through the S matrices, which in the flavor basis are governed by

$$i\frac{d}{dt}S(E) = (H_V(E) + H_e(t) + H_{\nu\nu}(t))S(E). \quad (2)$$

The vacuum Hamiltonian is given in the flavor basis by

$$H_V(E) = U_{23}(\theta_{23})U_{13}(\theta_{13})U_{12}(\theta_{12})\begin{pmatrix} -\Delta_{21}(E) & 0 & 0 \\ 0 & \Delta_{21}(E) & 0 \\ 0 & 0 & (\Delta_{31}(E) + \Delta_{32}(E)) \end{pmatrix} U_{12}^{\dagger}(\theta_{12})U_{13}^{\dagger}(\theta_{13})U_{23}^{\dagger}(\theta_{23}), \quad (3)$$

where $\Delta_{ij}(E) = (m_i^2 - m_j^2)/(4E)$ and the $U_{ij}(\theta_{ij})$s are the unitary matrices that take the Hamiltonian from the mass basis where $H_V(E)$ is diagonal to the flavor basis. The matter potential influencing neutrino oscillations is $V_e(t) = \sqrt{2}G_F N_e(t)$, where G_F is the Fermi constant. The matter potential results in Hamiltonian contribution, $H_e(t)$,

$$H_e(t) = \begin{pmatrix} V_e(t) & 0 & 0 \\ 0 & 0 & 0 \\ 0 & 0 & 0 \end{pmatrix}. \quad (4)$$

Neutrinos also feel a potential from interacting with other neutrinos often called the self-interaction potential. This

potential is computed similarly, but because the neutrinos are not isotropically distributed above the disk, the test neutrino will feel a nontrivial geometric effect from the other neutrinos. The resulting Hamiltonian contribution is $H_{\nu\nu}(t)$,

$$H_{\nu\nu}(t)$$
$$= \int_0^{\infty} (S(t,E)\rho(t,E)S^{\dagger}(t,E) - \bar{S}^*(t,E)\bar{\rho}(t,E)\bar{S}^T(t,E))dE. \quad (5)$$

Initially S is the identity matrix but evolves according to Eq. (2) as the neutrinos oscillate. The matrices, ρ and $\bar{\rho}$, take the form

$$\rho(t,E) = \sqrt{2}G_F \begin{pmatrix} \phi_{\nu_e}(E)C_{\nu_e}(t) & 0 & 0 \\ 0 & \phi_{\nu_\mu}(E)C_{\nu_\mu}(t) & 0 \\ 0 & 0 & \phi_{\nu_\tau}(E)C_{\nu_\tau}(t) \end{pmatrix}$$

$$\bar{\rho}(t,E) = \sqrt{2}G_F \begin{pmatrix} \phi_{\bar{\nu}_e}(E)C_{\bar{\nu}_e}(t) & 0 & 0 \\ 0 & \phi_{\bar{\nu}_\mu}(E)C_{\bar{\nu}_\mu}(t) & 0 \\ 0 & 0 & \phi_{\bar{\nu}_\tau}(E)C_{\bar{\nu}_\tau}(t) \end{pmatrix}, \quad (6)$$

where $C_a(t)$ is the geometric contribution and the $\phi_a(E)$ is the flux for the $a = \nu_e, \nu_\mu, \nu_\tau, \bar{\nu}_e, \bar{\nu}_\mu, \bar{\nu}_\tau$ disk. The geometric contribution was derived in Ref. [18] for a disk in general. Since we are calculating trajectories like those in Fig. 1, which make a 45° angle with the plane of the disk, we can reduce this general expression to

$$C_a(t) = \frac{-x}{2\pi}\int_{R_{\text{inner}}}^{R_a} C(r,x)rdr, \quad (7)$$

where

$$C(r,x) = \frac{\pi 4x^3}{\sqrt{2}(lm)^{3/2}} - \frac{2\mathcal{E}(\frac{m-l}{m})}{\sqrt{ml}}, \quad (8)$$

with R_a as the radius of the disk, E as the (anti)neutrino energy, $l = (x-r)^2 + x^2$, $m = (x+r)^2 + x^2$, $\mathcal{E}(M)$ as the complete elliptic integral of the second kind, and x as the distance from the center along the plane of the disk.

We take the fluxes of neutrinos and antineutrinos to have the spectrum of the Fermi Dirac flux with zero chemical potential so that for electron neutrinos or electron antineutrinos with temperature, T, the flux is

$$\phi_{\nu_e(\bar{\nu}_e)}(E) = \frac{gc}{2\pi^2(\hbar c)^3}\frac{E^2}{1+e^{T/E}}, \quad (9)$$

where $g = 1$ is the spin parameter. For $\nu_\mu(\bar{\nu}_\mu)$ and $\nu_\tau(\bar{\nu}_\tau)$ with temperature, T, the flux is also taken to have a Fermi Dirac

spectrum with zero chemical potential. However, for the case of the single radius model, the flux is rescaled by f_0,

$$\phi_a(E) = f_0 \frac{gc}{2\pi^2(\hbar c)^3} \frac{E^2}{1 + e^{T/E}}, \qquad (10)$$

where $a = \nu_\mu, \bar{\nu}_\mu, \nu_\tau$ or $\bar{\nu}_\tau$. For the multiple radius model, the flux is not rescaled, so $f_0 = 1$, and the amount of $\nu_\mu, \bar{\nu}_\mu, \nu_\tau$, and $\bar{\nu}_\tau$ flux is entirely determined by the disk radius and temperature. Initially, the system has the same flux of $\nu\mu, \nu_\tau$, $\bar{\nu}_\mu$, and $\bar{\nu}_\tau$ from each flavor, and these neutrinos all have the same emission geometry. Thus the density matrices can be written as

$$\rho(t, E) = \sqrt{2}G_F \begin{pmatrix} \phi_{\nu_e}(E)C_{\nu_e}(t) & 0 & 0 \\ 0 & \phi_{\nu_\mu}(E)C_{\nu_\mu}(t) & 0 \\ 0 & 0 & \phi_{\nu_\mu}(E)C_{\nu_\mu}(t) \end{pmatrix}$$

$$\bar{\rho}(t, E) = \sqrt{2}G_F \begin{pmatrix} \phi_{\bar{\nu}_e}(E)C_{\bar{\nu}_e}(t) & 0 & 0 \\ 0 & \phi_{\nu_\mu}(E)C_{\nu_\mu}(t) & 0 \\ 0 & 0 & \phi_{\nu_\mu}(E)C_{\nu_\mu}(t) \end{pmatrix}. \qquad (11)$$

At $t = 0$, the part of the Hamiltonian that comes from the neutrino self-interaction, $H_{\nu\nu}$ [Eq. (5)], has only one nonzero element which is the eeth element. We define this to be $V_\nu(t)$,

$$V_\nu(t) = V_{\nu_e}(t) - V_{\bar{\nu}_e}(t)$$
$$= \sqrt{2}G_F \int_0^\infty (C_{\nu_e}(t)\phi_{\nu_e}(E) - C_{\bar{\nu}_e}(t)\phi_{\bar{\nu}_e}(E))dE. \qquad (12)$$

Sometimes it is instructive to examine the unoscillated potential, i.e. what the self-interaction potential would be if no oscillations were to occur. We will use V_ν for this purpose. Of course, as neutrinos oscillate, the self-interaction potential does evolve. The S matrices of Eq. (5) gain of-diagonal components, and therefore so does $H_{\nu\nu}$. The potential in the eeth component deviates from Eq. (12), and we define

$$V_{\text{osc}} = (H_{\nu\nu})_{ee} - \text{Tr}(H_{\nu\nu})/3. \qquad (13)$$

Before calculating the neutrino flavor transformation above our two types of disk configurations, we compute the unoscillated self-interaction potential, $V_\nu(t)$, using the values for R_a and T_a from Tables I and II. We show the results in Figs 2(a) and 3(a)) for the magnitudes of all the potentials, $\Delta_{12}, |\Delta_{32}|, V_e(t)$, and $|V_\nu(t)|$. Figure 2(a) is computed for the single radius model (Table I), and Fig. 3(a) is computed for the multiple radius model (Table II). The vacuum potentials, Δ_{12}, and $|\Delta_{32}|$, are plotted with a dark green dotted line and light green finely dotted line, respectively. These vacuum potentials in the figure have a neutrino energy of $E = 20$ MeV. The self-interaction potential, $|V_\nu(t)|$, is plotted in a dashed light blue line. The horizontal axis in all plots is progress along the neutrino trajectory in cm. Since we use trajectories that are at a 45° angle, the progress along the trajectory is $\sim\sqrt{2}x$.

Close to the disk, at the start of the trajectory, the geometric effect on the self-interaction potential varies little. At these distances, where the scale of the disk is large compared to the distance of the neutrino from the disk, the geometric contributions of neutrinos and antineutrinos are similar: $C_{\bar{\nu}_e} \sim C_{\nu_e}$ and roughly constant. The hotter antineutrino disk will contribute more flux ($\phi_{\bar{\nu}_e} > \phi_{\nu_e}$), and this higher antineutrino emission causes the self-interaction potential to start out negative. Far from the disk, the geometric contribution to the self-interaction potential has the form

$$C_a(t) \sim \frac{3(R_a^4 - R_{\text{inner}}^4)}{256\sqrt{2}x(t)^4}. \qquad (14)$$

The turnover between these two behaviors is determined by the disk radius, R_a. In the single disk model of Fig. 2, this turnover happens at about $x_{\text{turn}} \sim 10^6$ cm because all flavors have the same geometry, with $R_a = 4.5 \times 10^6$ cm for all a. While we are using a 45° trajectory for ease of computation, this generic behavior of the geometric factor will be common to trajectories in all directions. Initially, the geometric factor will be roughly constant, and later it will decline as $1/r^4$. The overall scale of the geometric factor for trajectories in different directions can vary by a small factor, typically around 2 for most trajectories of interest, and the behavior in the intermediate regime can take a slightly different form. We caution that the calculations presented in the following sections are done in the "single angle" approximation, meaning that neutrinos coming from all directions are assumed to have the same history; i.e. it is assumed that they have always encountered the same potentials. Multiangle calculations, e.g. Refs. [38,46], would relax that approximation. Of particular relevance to MNR transitions discussed here, neutrinos arriving at the same point will have slightly different geometric factors, and thus the turnover points could be slightly different, and so the resonances
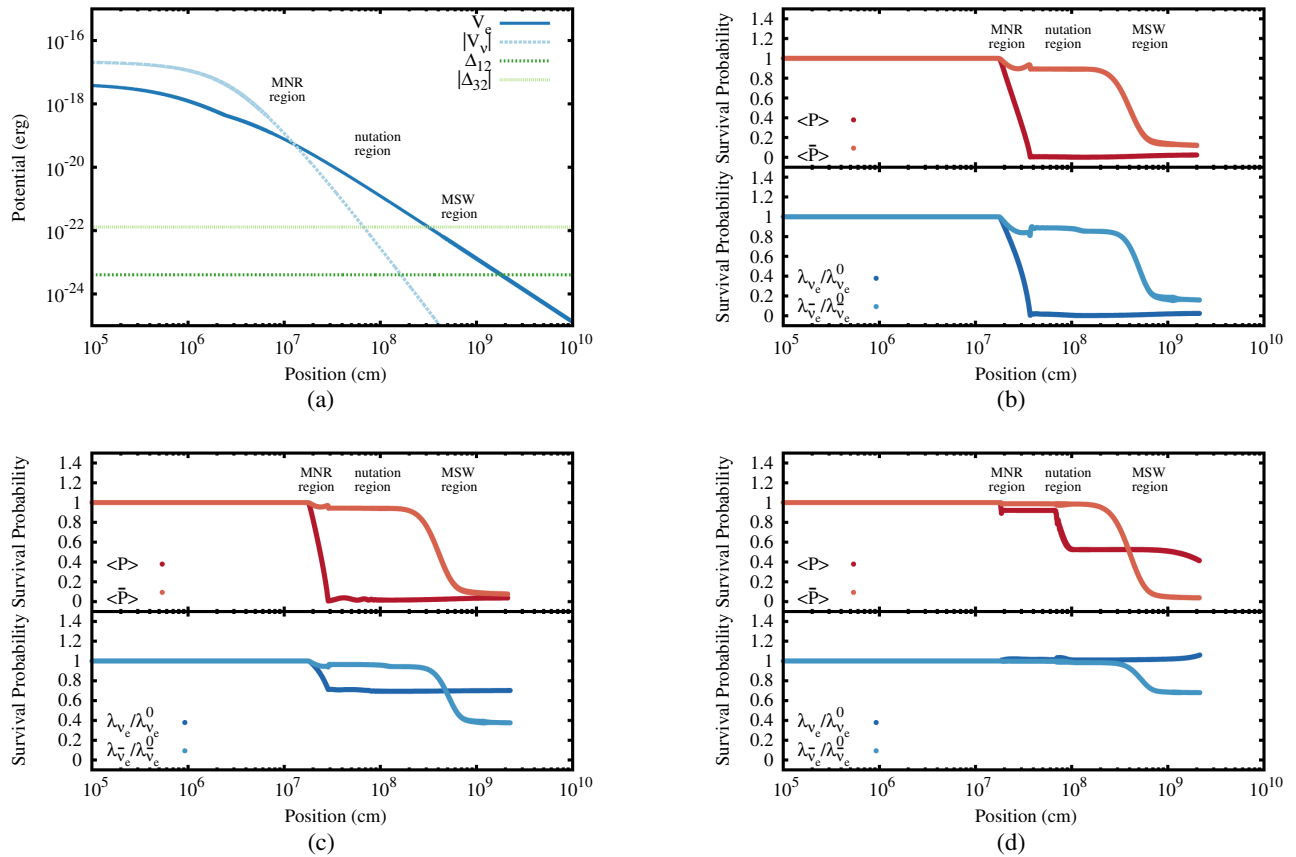
FIG. 2.   Single disk model: All flavors of neutrinos and antineutrinos are emitted from a disk of the same size. The neutrino and antineutrino temperatures differ, as in Table I. The horizontal axis in all plots is progress along the neutrino trajectory in cm. (a) Potentials entering the Hamiltonian from electrons as in Eq. (4) and from neutrinos as in Eq. (12) in the absence of oscillation. *All other plots:* The top panel shows the flux weighted electron neutrino survival probability, $\langle P \rangle$, in red solid lines and the flux weighted electron antineutrino survival probability, $\langle \bar{P} \rangle$, in the dashed amber line. In the bottom panel, we show the relative capture rates of the electron neutrinos and antineutrinos. The relative capture rate of the neutrinos is a ratio of the electron neutrino capture rate when oscillations are taken into account, λ_{ν_e}, to the electron neutrino capture rate when oscillations are not present, $\lambda_{\nu_e}^0$, and is shown as the dark blue line. The relative electron antineutrino capture rate is the analogous ratio, $\lambda_{\bar{\nu}_e}/\lambda_{\bar{\nu}_e}^0$, which we show in a light blue dashed line. (b) No mu or tau neutrinos are emitted from the disk. (c) Mu and tau neutrino fluxes are rescaled; $f_0 = 0.35$ relative to their blackbody fluxes. (d) Mu and tau neutrino fluxes are rescaled; $f_0 = 0.75$.

locations could be different. If the resonances are in similar spatial locations, one expects little effect, but if they are quite different, then this may change the nature of the transition.

In the multiple disk model of Fig. 3(a), a similar turnover in the potential would occur at about $x_{\text{turn}} \sim 10^6$ cm as well. However, because the disks for electron neutrinos and antineutrinos have different radii, there is an additional feature. At $x_{\text{sym}} \sim 10^6$ cm, the neutrino self-interaction potential for the multiple radius disk shows a symmetric point where the self-interaction potential goes through zero, at the place where the electron neutrino and electron antineutrino contributions to the self-interaction potential are the same. This symmetric point is a consequence of the nontrivial geometric contribution to the self-interaction potential [Eq. (7)] and the differing electron neutrino and electron antineutrino radii and temperatures.

Again, the electron antineutrino disk is hotter than the electron neutrino disk, and the local emission surface produces more flux,

$$\int_0^\infty \phi_{\nu_e}(E)dE < \int_0^\infty \phi_{\bar{\nu}_e}(E)dE, \qquad (15)$$

regardless of the local behavior of the geometric factors, $C_{\bar{\nu}_e}(t)$ and $C_{\nu_e}(t)$. Close to the disk surface, the disk sizes are less important in determining the self-interaction potential [Eq. (12)] than the temperatures since the geometric contributions are essentially the same and constant. Therefore the self-interaction potential will be negative and stay roughly constant close to the emission surface as can be seen in Figs. 2(a) and 3(a).

While the flux of the electron antineutrinos always dominates over the flux of the electron neutrinos
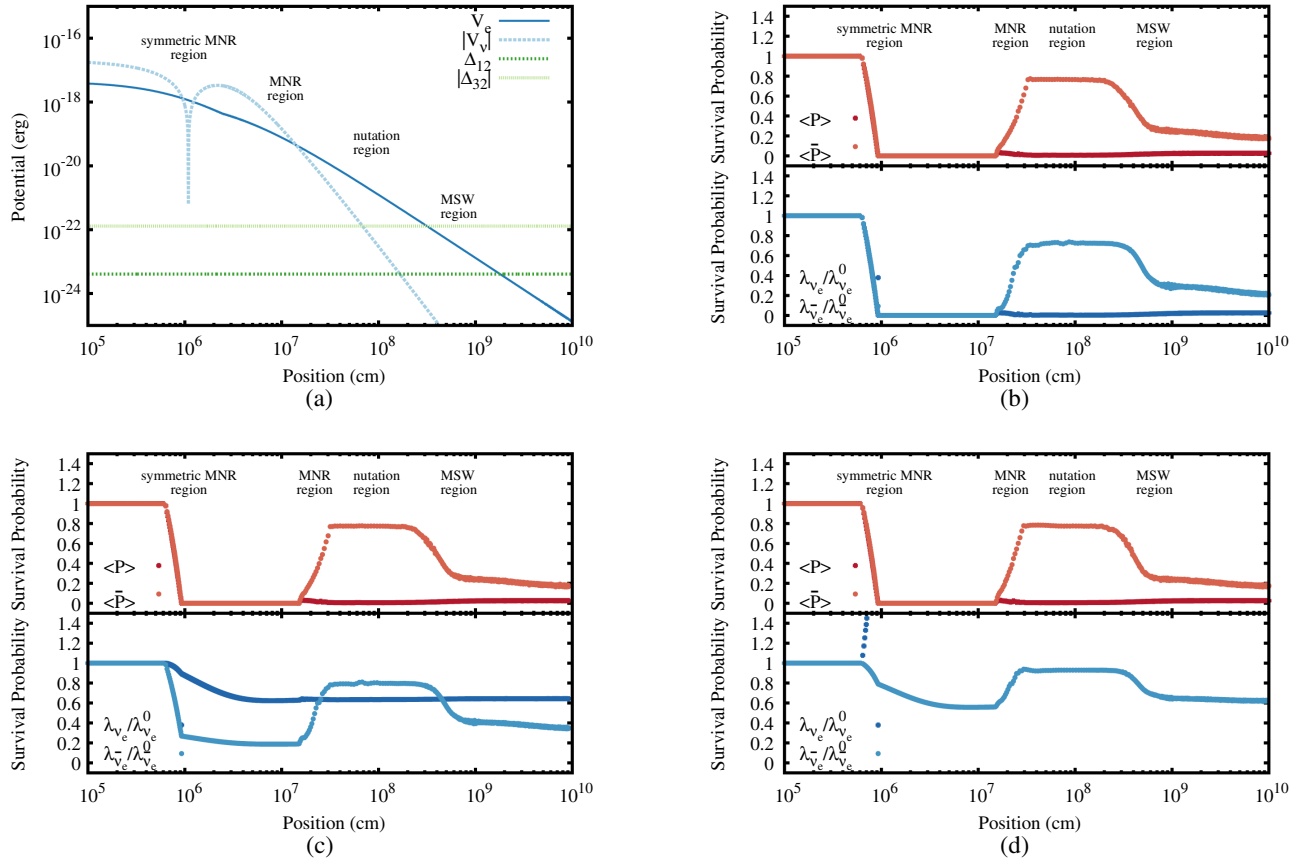
FIG. 3. Multiple disk model: Different flavors of neutrinos and antineutrinos are emitted from disks of different sizes, as in Table II, i.e. $R_{\nu_e} = 5.2 \times 10^6$ cm and $R_{\bar{\nu}_e} = 3.9 \times 10^6$ cm. The horizontal axis in all plots is progress along the neutrino trajectory in cm. (a) Potentials entering the Hamiltonian from electrons as in Eq. (4) and from neutrinos as in Eq. (4) in the absence of oscillation. *All other plots:* The top panel shows the flux weighted electron neutrino survival probability, $\langle P \rangle$, in red solid lines and the flux weighted electron antineutrino survival probability, $\langle \bar{P} \rangle$, in dashed amber line. In the bottom panel, we show the relative capture rates of the electron neutrinos and antineutrinos. The relative capture rate of the neutrinos is a ratio of the electron neutrino capture rate when oscillations are taken into account, λ_{ν_e}, to the electron neutrino capture rate when oscillations are not present, $\lambda_{\nu_e}^0$, in a dark blue line. The relative electron antineutrino capture rate is the analogous ratio, $\lambda_{\bar{\nu}_e}/\lambda_{\bar{\nu}_e}^0$, which we show in a light blue dashed line. (b) No mu and tau neutrinos or antineutrinos are emitted. (c) Mu and tau neutrinos and antineutrinos are emitted from a disk with radius of 1.8×10^6 cm. (d) Mu and tau neutrinos and antineutrinos are emitted from a disk with a radius of 2.4×10^6 cm.

everywhere on the trajectory, farther from the disk surface, as the disk sizes become important, the self-interaction geometric contribution associated with the neutrinos becomes larger than the geometric contribution associated with the antineutrinos, $C_{\bar{\nu}_e}(t) < C_{\nu_e}(t)$. This occurs because the radii, R_a, that set the scale of the potentials' turnover are different, $R_{\bar{\nu}_e} < R_{\nu_e}$, so the geometric contribution for the electron antineutrinos begins to decrease sooner than the geometric contribution for the electron neutrinos [Eq. (14)]. The symmetric point at about $x_{\text{sym}} \sim 10^6$ cm is the place where the two potentials are the same magnitude and sum to zero. Before this point V_ν is negative, and after it V_ν becomes positive.

The matter potential, which is shown as the light blue line in Figs. 2(a) and 3(a), depends on the mass density of material in the outflow and the electron fraction. The matter close to the disk where the outflow trajectory would be

vertical stays at a relatively constant density, which we take to be close to 10^{10} g/cm^3. As the outflow enters the radial trajectory, where we begin our calculation, the matter expands, dropping the density to roughly 10^8 g/cm^3. After this turnover, as the mass streams far from the disk, it continues a decline in density, calculated assuming a constant mass outflow rate as described in Sec. II.

Before embarking on the neutrino flavor transformation calculation, we can use the (unoscillated) potentials plotted in Figs. 2(a) and 3(a) to identify regions where various types of oscillation physics may take place. In the single disk model, Fig. 2(a), at the beginning of the trajectory, the matter potential, in a dark blue line, and the size of the self-interaction potential, in the light blue line, are large. The large self-interaction potential corresponds to synchronized neutrino oscillations where all modes behave roughly the same way, even though they have different energies. After

the synchronized region, the matter potential and the neutrino self-interaction potential have the same magnitude at 2×10^7 cm creating a matter neutrino resonance region. At about 10^8 cm where the neutrino self-interaction scale and the vacuum scale are roughly the same size, there is a nutation region, and at about 3×10^8 cm, there is a MSW regime. The multiple disk model, Fig. 3, has these regions of interest at more or less the same places and an additional matter neutrino resonance region at $x_{\text{sym}} \sim 10^6$ cm due to the symmetric point.

IV. RESULTS

We now wish to consider the oscillation of neutrinos for the models discussed in the previous two sections. We perform the calculations outlined in Sec. III for each of our models with varying contributions from ν_μ, ν_τ, $\bar{\nu}_\mu$, and $\bar{\nu}_\tau$. We take the vacuum mixing parameters to be consistent with the current values of the Particle Data Group [47], $\theta_{12} = 34.4°$, $\theta_{13} = 9°$, $\theta_{23} = 45°$, $\Delta_{12}E = 7.59 \times 10^{-5}$ eV^2, and $|\Delta_{23}E| = 2.43 \times 10^{-3}$ eV^2. We use the inverted hierarchy although the matter-neutrino resonances are nearly hierarchy independent, and we find very similar results for these transitions in the normal hierarchy. The self-interaction Hamiltonian couples the neutrinos and antineutrinos of different energies together, and our integration keeps track of 800 different neutrino energies between 1 and 101 MeV.

$$\lambda_{\nu_e} = \frac{\pi c G_F^2}{(\hbar c)^4}(c_V^2 + 3c_A^2) \int_0^\infty (\phi'_{\nu_e}(r,E)P_{\nu_e \to \nu_e}(E) + \phi'_{\nu_\mu}(r,E)P_{\nu_\mu \to \nu_e}(E) + \phi'_{\nu_\tau}(r,E)P_{\nu_\tau \to \nu_e}(E))(E+Q)^2 dE$$

$$\lambda_{\bar{\nu}_e} = \frac{\pi c G_F^2}{(\hbar c)^4}(c_V^2 + 3c_A^2) \int_{E_0}^\infty (\phi'_{\bar{\nu}_e}(r,E)P_{\bar{\nu}_e \to \bar{\nu}_e}(E) + \phi'_{\bar{\nu}_\mu}(r,E)P_{\bar{\nu}_\mu \to \bar{\nu}_e}(E) + \phi'_{\bar{\nu}_\tau}(r,E)P_{\bar{\nu}_\tau \to \bar{\nu}_e}(E))(E-Q)^2 dE, \quad (18)$$

where $Q = m_n - m_p$ is the nucleon mass difference and $E_0 = (m_n - m_p + m_e)$ is the threshold energy for electron antineutrino capture. The fluxes, $\phi'_a(r,E)$, decrease appropriately as the distance from the disk increases [this geometric effect is described in Ref. [6] and is different from $\phi_a(E)C_a$]. In addition to plotting survival probabilities, we will plot the ratio of the capture rates in the case with neutrino oscillations to the case without neutrino oscillations. In the absence of oscillation, the capture rates, $\lambda_{\nu_e}^0$ and $\lambda_{\bar{\nu}_e}^0$, are calculated with

$$P_{\nu_e \to \nu_e}(E) = 1$$
$$P_{\nu_\mu \to \nu_e}(E) = 0$$
$$P_{\nu_\tau \to \nu_e}(E) = 0$$
$$P_{\bar{\nu}_e \to \bar{\nu}_e}(E) = 1$$
$$P_{\bar{\nu}_\mu \to \bar{\nu}_e}(E) = 0$$
$$P_{\bar{\nu}_\tau \to \bar{\nu}_e}(E) = 0, \quad (19)$$

for all energies, E.

The result of the calculation is the S matrices, which we use to find the flux weighted survival probabilities,

$$\langle P \rangle = \frac{\int_0^\infty \phi_{\nu_e}(E) P_{\nu_e \to \nu_e}(E) dE}{\int_0^\infty \phi_{\nu_e}(E) dE}$$

$$\langle \bar{P} \rangle = \frac{\int_0^\infty \phi_{\bar{\nu}_e}(E) P_{\bar{\nu}_e \to \bar{\nu}_e}(E) dE}{\int_0^\infty \phi_{\bar{\nu}_e}(E) dE}. \quad (16)$$

The energy dependent survival probabilities and transition probabilities come from the S matrix,

$$P_{\nu_e \to \nu_e}(E) = |S_{ee}(E)|^2$$
$$P_{\nu_\mu \to \nu_e}(E) = |S_{\mu e}(E)|^2$$
$$P_{\nu_\tau \to \nu_e}(E) = |S_{\tau e}(E)|^2$$
$$P_{\bar{\nu}_e \to \bar{\nu}_e}(E) = |\bar{S}_{ee}(E)|^2$$
$$P_{\bar{\nu}_\mu \to \bar{\nu}_e}(E) = |\bar{S}_{\mu e}(E)|^2$$
$$P_{\bar{\nu}_\tau \to \bar{\nu}_e}(E) = |\bar{S}_{\tau e}(E)|^2. \quad (17)$$

The evolution matrix, $\bar{S}$, for the antineutrinos obeys an equation similar to Eq. (2).

The capture rates for electron neutrinos and antineutrinos on neutrinos and protons, respectively, are approximated as

A. Single disk models

We first present the results of the calculations described in Sec. III using the single disk model discussed in Sec. II. We calculate the neutrino oscillation pattern resulting from these potentials and show the results in Figs 2(b), 2(c), and 2(d) for different amounts of emitted mu and tau neutrinos and antineutrinos.

The potentials in Fig. 2(a) shape the oscillation regions that the neutrinos enter by their relative sizes. The matter potential and the self-interaction potential become the same size at 2×10^7 cm. We identify this position as a standard MNR region. Standard MNR transitions have been explained in Ref. [19] and have similarities with the neutrino-antineutrino transformation discussed in Ref. [48]. In a standard MNR transition, the self-interaction potential from Eq. (13) changes so that it matches the size of the matter potential throughout the transition: $|V_e| \sim |V_{\text{osc}}|$. This means that the on-diagonal component of H stays near zero, i.e.

$$V_{\text{osc}} + V_e + (H_V)_{ee} \sim 0. \quad (20)$$

If the system is sufficiently adiabatic, a standard MNR transition will occur: neutrinos and antineutrino oscillate in just such a way that the potentials maintain the resonance. The oscillated V_{osc} changes to enforce Eq. (20). As discussed in Ref. [19], the behavior of this resonance transition is well approximated by a single monoenergetic neutrino and antineutrino model. In this context, Ref. [19] derived the diabaticity criteria that come from matching the time scale of transition determined by the scale height, $\tau = |d\log(V_e/V_{\nu_e})/dl|^{-1}$, of the matter and self-interaction potentials,

$$\delta l_1 = \tau \log\left(\frac{\alpha+1}{\alpha-1}\right), \tag{21}$$

with the time scale determined by the capacity of the system to change flavor,

$$\delta l_2 = \frac{-1}{\Delta \sin 2\theta S_{\text{ext}}}, \tag{22}$$

where

$$\alpha \equiv \frac{V_{\bar{\nu}_e}(t)}{V_{\nu_e}(t)} \tag{23}$$

and S_{ext} is the average difference between the y components of neutrino flavor isospin vectors for the neutrino and antineutrino [19], which must be less than $(1+\alpha)/2$. Below this value, $\delta l_1 = \delta l_2$ as long as θ is sufficiently large. For the single disk model, the scale height is $\tau_{\text{single}} \sim 7 \times 10^6$ cm at the standard MNR region, where $\alpha \sim 1.4$. These values mean that, in order for a transition to occur associated with δm_{13}^2, the mixing angle must be $\theta > 3 \times 10^{-2}$. The measured mixing angle, $\theta_{13} \sim 0.2$, is well within that range. The standard MNR regions in our models should be sufficiently adiabatic to sustain transitions.

We now look at our numerical calculations to see if the transitions indeed occur. The results of these calculations are shown in Figs. 2(b), 2(c), and 2(d). If there are no mu or tau neutrinos and antineutrinos, the transition results in a flux weighted survival probability for electron neutrinos dropping to nearly zero and the flux weighted survival probability of electron antineutrinos returning to nearly 1, as in Fig. 2(b). This is the characteristic behavior of a standard MNR described in Ref. [19]. The relative capture rates of electron neutrinos are shown in solid dark blue, and electron antineutrinos are shown in light dashed blue lines in the lower panel. Because no mu or tau neutrinos are present initially, these relative capture rates track closely to the weighted survival probabilities.

Increasing the initial amount of mu and tau neutrinos by a small amount has little effect on the survival probabilities but a significant effect on the capture rates. This can be seen in Fig. 2(c) where a small quantity of mu and tau neutrinos

is now emitted from the disk. The number flux of each of these types of neutrinos and neutrinos is slightly under 40% of the electron antineutrino flux. We see from a comparison of the top panel of Figs. 2(b) and 2(c) that the addition of the mu and tau neutrinos at this modest level changes the survival probabilities very little. However, a comparison of the bottom panels shows that the relative capture rates have changed. Both the relative capture rates of electron neutrinos and of the electron antineutrinos begin at 1, like the weighted survival probability. During the MNR, the capture rate of electron neutrinos drops only to about 70%. The small change in the capture rate occurs despite the fact that the MNR results in a strong transition from initially electron flavor neutrinos to other flavors, because mu and tau neutrinos *also* transform at the MNR to the electron flavor.

Increasing the initial amount of mu and tau neutrinos by a larger amount than in Fig. 2(c) has a more dramatic effect. In Fig. 2(d), where the mu and tau neutrino flux is 85% of the electron antineutrino component, the top panel shows that neutrinos initially in the electron flavor remain in the electron flavor, even as they pass through the MNR region. The bottom panel of Fig. 2(d) is consistent with this failure of the MNR to result in transition; the capture rate of electron neutrinos remains the same, just as if there were no MNR region. This behavior occurs generically when the mu and tau fluxes approach the same level as the electron neutrinos and antineutrinos. During MNR transitions, the neutrinos and antineutrinos transform in such a way so that the self-interaction potential matches the matter potential, Eq. (20). But since a neutrino flavor transformation involves a trading of electron-type neutrinos with mu- and tau-type neutrinos, if there are similar numbers of electron neutrinos as other types, then the self-interaction potential, Eq. (13), cannot change much, and no transformation occurs.

After the MNR region, the system passes through a nutation region, which happens at about 10^8 cm in Figs. 2(b), 2(c), and 2(d). Nutation oscillations are a high neutrino density phenomenon that have been deeply studied in the supernova setting, e.g. Refs. [30]. They have also been studied in the disk setting [17,18]. They occur when the self-interaction potential approaches the size of the vacuum scale, and a required initial condition is that the electron neutrinos and antineutrinos begin approximately in their flavor eigenstates. During the transition, the neutrinos and antineutrinos are said to be locked in that their transition probabilities are linked. The transitions are largest in the inverted hierarchy which is the case for the calculations presented here. In Figs. 2(b), 2(c), and 2(d) the nutation region occurs after the matter neutrino resonance region which would be a typical expectation in a disk system. These figures show that nutation oscillations occur only in the case where MNR transitions do not, i.e. Fig. 2(d). This is because the MNR transition moves the

electron neutrinos and antineutrinos out of their initial eigenstates, and the required initial conditions for a nutation oscillation are not met. We note that nutation oscillations have been shown to depend upon multiangle effects which are expected to be large in a disk setting. The authors of Ref. [17] discussed a formalism by which to use a single angle calculation to find nutation oscillation survival probabilities that are robust in a merger.

A MSW region occurs when the matter potential becomes the same size as the vacuum scale. In the models of Figs. 2(b), 2(c), and 2(d), this region is at about 4×10^8 cm. At the densities where MSW regions occur, the self-interaction potential tends to be small, and the neutrinos and antineutrinos of different energies act almost independently. The energy dependent oscillations will then occur only if the system is sufficiently adiabatic. In all three examples, we see that the MSW regime results in transitions of the electron antineutrinos to other flavors. These transitions of electron antineutrinos would not be possible in the normal hierarchy where instead electron neutrinos would transform.

B. Multiple disk model

In the multiple disk model, neutrinos of different flavors are emitted from disks of different radii as given in Table II. There are three different emission surfaces, one for electron neutrinos, one for electron antineutrinos, and one for all other flavors. The potentials for this model are shown in Fig. 3(a), and the different regions of oscillation behavior were discussed in Sec. III. In this section we discuss the results of the multiple disk model calculations, which are shown in Figs. 3(b), 3(c), and 3(d).

Initially, the multiple disk models behave in the same way as the single disk models and have a region of synchronized behavior close to the disk, so that the survival probability is essentially 1 in the region before $\sim 10^6$ cm. However, after this point the multiple disk models start to exhibit a differences with the single disk models because they enter the symmetric MNR region which does not exist in the single disk model. In the symmetric MNR region, V_{osc} from Eq. (13) becomes the same size as V_e. As discussed in Sec. III, in the multiple disk models, the difference in the changing geometric factors causes the self-interaction potential V_ν, that would otherwise have large magnitude, to sweep through zero. We call this a symmetric resonance region because it occurs close to the point where $\alpha = 1$. The transitions in this region are similar to those observed in Ref. [18], and the phenomenology of these transitions has similarities to the standard MNR [19]. In all three of Figs. 3(b), 3(c), and 3(d), both neutrinos and antineutrinos undergo a nearly complete transformation.

The mu and tau neutrinos can prevent the MNR transition if their flux becomes roughly the same as the electron neutrinos and antineutrinos. This case was shown in the single disk model in Fig. 2(d). However, in all the multidisk examples, the mu and tau neutrinos are either nonexistent as in Fig. 3(b) or emitted from a smaller disk than the ν_e and $\bar\nu_e$, $R_{\nu_\mu} = 1.8 \times 10^6$ cm in Fig. 3(c) and $R_{\nu_\mu} = 2.4 \times 10^6$ cm in Fig. 3(d). Therefore, they do not give roughly the same contribution as the electron-type neutrinos and antineutrinos at the position of the resonance, and the transition can proceed.

While the presence of a relatively modest number of mu and tau neutrinos does not effect the survival probability of the electron neutrinos and antineutrinos at the symmetric matter neutrino resonance, they do alter the capture rates. This is again because the electron neutrinos do not simply "oscillate away"; instead they exchange places with the mu/tau type. For example, the lower panel of Fig. 3(c) shows in the blue solid line the relative capture rate of electron neutrinos, which drops from 1 to only about 0.6 at the symmetric matter neutrino resonance transition. In the lower panel of Fig. 3(d), where the mu and tau contributions are a little larger, the electron neutrino capture rate is *higher* than if there had been no transformation at all. This is due to the higher energy of the mu and tau neutrinos at emission and the energy squared dependence of the neutrino capture cross section.

After the symmetric matter neutrino resonance transition, the neutrinos encounter a standard MNR region at about 2×10^7 cm in Figs 3(b), 3(c), and 3(d). Whether or not a standard MNR transition occurs depends on the state of the system as it enters the standard MNR region. Transitions cannot occur unless the resonance condition, Eq. (20), is fulfilled, and for this to happen the neutrino self-interaction potential must be negative. While the potential, V_ν, begins negative close to the disk, the changing geometric factors cause a relative sign change in the potential [see Eq. (12)] so that V_ν is positive at the position of the standard MNR. However, V_ν is what the self-interaction potential would be in the absence of oscillations. The system has already undergone a transformation at the symmetric MNR, and this transition produces an *additional* change in the sign so that the actual self-interaction potential, V_{osc}, is negative. Thus, if a symmetric MNR transition occurs, the system is set up favorably for a standard MNR transition. Since in all our examples a symmetric MNR transition occurs, we expect a standard MNR transition as well. The change in survival probability at the standard MNR region can be seen in the top panels of Figs. 3(b), 3(c), and 3(d) to follow the typical behavior of a standard MNR transition. Similar to the single disk model, the standard MNR transitions have a nontrivial effect on the capture rates as can be seen in the bottom panels of these figures.

After the MNR regions, the neutrinos encounter the nutation region at about 10^8 cm. As in the single disk models, Figs. 2(b) and 2(c), the system is no longer in the original flavor eigenstates, and the nutation region results in no flavor transformation. The neutrinos then enter a MSW

region after several times 10^8 cm, where some flavor transformation takes place in Figs 3(c), 3(c), and 3(d). Also, as in the single disk case, since we are using the inverted hierarchy, the electron antineutrinos in the multiple disk case transform to other flavors at the MSW region.

V. NUCLEOSYNTHESIS

The symmetric MNR region shown in Fig. 3 occurs quite close to the disk and thus will impact the element synthesis in outflowing material from the inner disk regions. This material starts out as primarily free nucleons, where neutrons far outnumber protons, and as it moves outward the composition evolves via the weak interactions

$$\nu_e + n \rightleftharpoons p + e^- \tag{24}$$

$$\bar{\nu}_e + p \rightleftharpoons n + e^+. \tag{25}$$
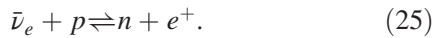
The approximate rates for the forward reactions are given in Eq. (18). In the nucleosynthesis calculations described in this section, we include also the weak magnetism contribution [49] to these rates. Since the disk emits more antineutrinos than neutrinos and the antineutrinos tend to be hotter, neutron-rich outflows are favored; the outflows may also retain some of the neutron richness of the disk. As the material expands and cools, the protons are quickly bound into alphas, and of the weak reactions above, only the top forward reaction, $\nu_e + n \rightarrow p + e^-$, continues to operate. The protons thus produced are promptly bound into alphas as well. At this stage of the nucleosynthesis, neutrinos act to increase the number of seed nuclei and reduce the number of free neutrons available for capture on the seeds. This is called the "alpha effect" [50,51], and it limits how far in A the nucleosynthesis can proceed. Most calculations of merger disk outflow nucleosynthesis [2,8,10,13,16,52,53] favor the production of weak ($80 < A < 120$), rather than main ($A > 120$), r process nuclei. The MNR can potentially alter this conclusion.

The influence of a MNR transition close to the emission surface on outflow nucleosynthesis was first pointed out for a collapsar-type disk in Ref. [18]. A collapsar disk emits primarily electron flavor neutrinos and antineutrinos, so when the MNR transition occurs, it is (from the perspective of the nuclear matter in the vicinity) as if the neutrinos disappear. If this happens in the region of the outflow where alphas are forming, the alpha effect can be cut off completely. With fewer seeds formed and more free neutrons remaining, a vigorous main r process can result [18].

Exactly how the MNR will influence merger outflow nucleosynthesis depends on the relative amounts of electron and mu/tau flavors emitted. If there is little mu/tau emission, we expect an effect similar to that described above for the collapsar case. This is shown in the dark/light blue lines in Figs. 4 and 5. Here, we start with the neutrino
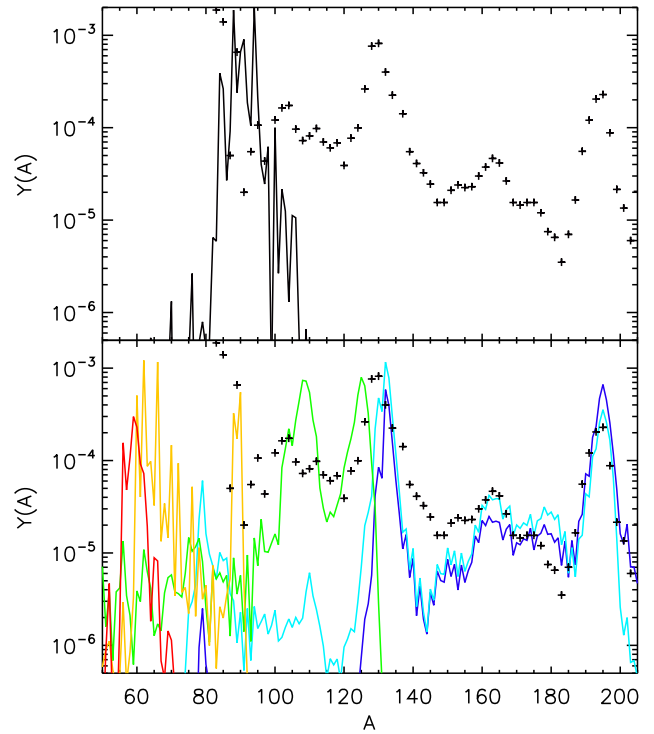

FIG. 4. Nucleosynthesis resulting from the multiple disk models. The vertical axis shows abundance, and the horizontal axis shows the mass number A of elements produced. *Both panels*: The black pluses show scaled solar r process residuals. *Top panel:* Production from the multiple disk model with no oscillations is shown in black. *Bottom panel:* Production from the multiple disk model with oscillation that includes no initial mu and tau neutrinos is shown in dark blue. Oscillation calculations where mu and tau neutrinos have a flux relative the electron antineutrinos at 5% (light blue), at 10% (green), at 20% (yellow), and at 65% (red) are shown.

emission from the multiple disk example, described in Sec. IV B, and calculate the element synthesis as in Refs. [13,18] along the outflow trajectory described in Sec. II. The top panel of Fig. 4 shows the final abundances for the case with no neutrino oscillations, compared to the solar r process abundance pattern. Primarily $A \sim 80 - 90$ neutron-rich nuclei are produced. The material starts out very neutron rich, as shown in the middle panel of Fig. 5, but the alpha effect limits the resulting nucleosynthesis to a weak r process. When the neutrino oscillations illustrated in Fig. 3 are included in the calculation, we find the MNR can radically change this picture. Figure 3(b) shows that the symmetric MNR region occurs at a point about 10 km along the outflow trajectory. If there are little to no mu/tau neutrinos to oscillate into the electron flavors, the electron neutrino capture rate will drop steeply in the MNR region. This is shown for example cases with little (light blue lines) to no (dark blue lines) mu/tau emission in the top panel of Fig. 5. For the outflow conditions considered here, MNR occurs just before the alphas start forming, as depicted in
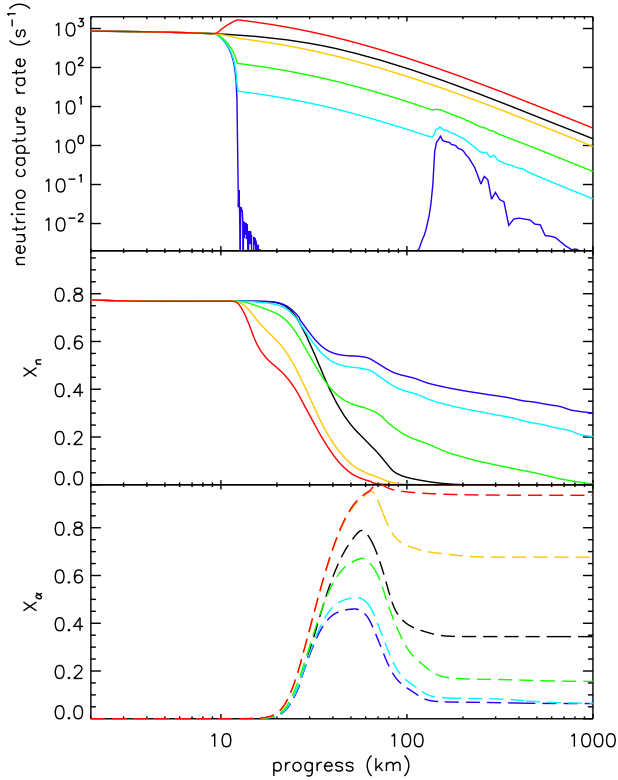
FIG. 5. *Top panel:* Neutrino capture rates from the multiple disk models as a function of position along the outflow trajectory. *Middle panel:* Neutron mass fraction as a function of position along the outflow trajectory. *Bottom panel:* Alpha particle mass fraction as a function of position along the trajectory. *All panels*: The multidisk model with no oscillations is shown in black. The multiple disk model with oscillation that includes no initial mu and tau neutrinos is shown in dark blue. Oscillation calculations where mu and tau neutrinos are included at 5% are shown in light blue, at 10% in green, at 20% in yellow, and at 65% in red.

the bottom panel of Fig. 5. Thus, the alpha effect is completely removed by the MNR—fewer alphas form (bottom panel of Fig. 5), more free neutrons remain (middle panel of Fig. 5), and a robust main r process results (bottom panel of Fig. 4).

If there is appreciable mu/tau emission from the disk, then the electron capture rates will not drop so steeply in the MNR region and may even increase, as described in Sec. IV and shown in Figs. 3(c) and 3(d). To explore this effect on the element synthesis, we repeat the oscillation and outflow calculations described above for increasing percentages. Since these are multiple disk calculations, we adjust the radius of the emission surface of the mu/tau neutrinos to 1.6×10^6, 1.8×10^6, and 2.4×10^6 cm, so that it corresponds to 10%, 20%, and 65% of mu/tau emission as compared with electron antineutrino emission. The results are shown in Figs. 4 and 5 by the green, yellow, and red lines, respectively. The symmetric MNR influences both the electron neutrino and antineutrino fluxes, effectively swapping them with hotter but weaker mu/tau fluxes. Thus,

for a short time before alphas form, the balance in the forward reaction rates of Eq. (25) is adjusted by the MNR, and the balance of protons and neutrons correspondingly shifts as shown in the middle panel of Fig. 5. In the 10% case, the neutrino capture rates still decrease, but there are enough electron neutrinos after the transition that a modest alpha effect occurs. This means that there are not enough neutrons for the r process to get all the way to the highest mass number nuclei, although the nucleosynthesis does proceed beyond the $A \sim 80$ r process peak region and some $A \sim 130$ peak nuclei are produced. In the 20% case, the neutrino capture rates are relatively unchanged, but the antineutrino capture rates are reduced, so that the overall composition is more proton rich than in the no oscillation case. This combined with a robust alpha effect results in a sharp reduction in $A \sim 80$ nucleosynthesis compared to the no oscillation case. With 65% mu/tau emission, the MNR results in *faster* neutrino capture rates, and the composition shifts to roughly equal numbers of neutrons and protons before alphas begin to form. Here, only iron peak nuclei result.

VI. CONCLUSIONS

Compact object mergers emit large numbers of neutrinos with a flux that is initially composed of more electron antineutrinos than neutrinos. This makes this environment a prime candidate for matter neutrino resonance transitions. There are two types of relevant neutrino emission configurations: one where all flavors of neutrinos are emitted from the same surface and one where neutrinos are emitted from different size surfaces. The latter is more in line with the results of recent compact object merger simulations. We find that two types of matter neutrino resonances occur. Both configurations show a standard MNR, which produces a transition where electron neutrinos wind up transformed into other flavors and electron antineutrinos wind up back in their initial eigenstates. We also find a symmetric MNR, where both electron neutrinos and antineutrinos are nearly completely transformed. The type of transition is a consequence of the behavior of the neutrino self-interaction potential which depends sensitively on the balance of ν_e and $\bar{\nu}_e$s.

The size of the initial contribution of mu- and tau-type neutrinos to the flux, as compared with electron antineutrinos and neutrinos, is crucial to determining whether a transition occurs or not. Comparable contributions will shut off the transition, but such large ν_μ and ν_τ fluxes are not currently predicted.

Future calculations of neutrino transport in mergers will be instrumental in determining what oscillation pattern we can expect above real world mergers, both because it is the balance of ν_e and $\bar{\nu}_e$s that determines the initial potential and also because the mu and tau fluxes determine the flexibility available to the system for a MNR transition. In addition the positions of the matter neutrino resonances are

affected by the interplay between the matter density and the neutrino potential. The neutrino potential changes slightly depending on the trajectory direction, but the matter potential can vary even more with the direction. Thus, different trajectories can experience the resonance at different locations. We will explore this effect in future work.

Matter neutrino resonance transitions have a significant impact on wind nucleosynthesis, because they occur when the neutrino self-interaction potential and matter potential are approximately balanced. If such transitions occur, they often occur close to the emission surface of the neutrinos, where the neutrinos still have large enough flux to affect the neutron to proton ratio, and nuclei in the outflow have not yet begun to form.

ACKNOWLEDGMENTS

[1] F. Foucart, M. B. Deaton, M. D. Duez, E. O'Connor, C. D. Ott, R. Haas, L. E. Kidder, H. P. Pfeiffer, M. A. Scheel, and B. Szilagyi, Phys. Rev. D **90**, 024026 (2014).

[2] A. Perego, S. Rosswog, R. M. Cabezon, O. Korobkin, R. Kappeli, A. Arcones, and M. Liebendorfer, Mon. Not. R. Astron. Soc. **443**, 3134 (2014).

[3] M. B. Deaton, M. D. Duez, F. Foucart, E. O'Connor, C. D. Ott, L. E. Kidder, C. D. Muhlberger, M. A. Scheel, and B. Szilagyi, Astrophys. J. **776**, 47 (2013).

[4] C. Palenzuela, S. L. Liebling, D. Neilsen, L. Lehner, O. L. Caballero, E. O'Connor, and M. Anderson, Phys. Rev. D **92**, 044045 (2015).

[5] H. Nagakura, K. Hotokezaka, Y. Sekiguchi, M. Shibata, and K. Ioka, Astrophys. J. **784**, L28 (2014).

[6] R. Surman and G. C. McLaughlin, Astrophys. J. **603**, 611 (2004).

[7] L. Roberts, S. Woosley, and R. Hoffman, Astrophys. J. **722**, 954 (2010).

[8] S. Wanajo, Y. Sekiguchi, N. Nishimura, K. Kiuchi, K. Kyutoku, and M. Shibata, Astrophys. J. **789**, L39 (2014).

[9] S. Goriely, A. Bauswein, O. Just, E. Pllumbi, and H.-T. Janka, Mon. Not. R. Astron. Soc. **452**, 3894 (2015).

[10] S.-Y. Wanajo and H.-T. Janka, Astrophys. J. **746**, 180 (2012).

[11] L. Dessart, C. Ott, A. Burrows, S. Rosswog, and E. Livne, Astrophys. J. **690**, 1681 (2009).

[12] R. Surman, G. McLaughlin, and W. Hix, Astrophys. J. **643**, 1057 (2006).

[13] R. Surman, G. McLaughlin, M. Ruffert, H.-T. Janka, and W. Hix, Astrophys. J. **679**, L117 (2008).

[14] O. Caballero, G. McLaughlin, and R. Surman, Phys. Rev. D **80**, 123004 (2009).

[15] A. Bauswein, R. A. Pulpillo, H. T. Janka, and S. Goriely, Astrophys. J. **795**, L9 (2014).

[16] O. Just, A. Bauswein, R. A. Pulpillo, S. Goriely, and H. T. Janka, Mon. Not. R. Astron. Soc. **448**, 541 (2015).

[17] B. Dasgupta, A. Dighe, A. Mirizzi, and G. G. Raffelt, Phys. Rev. D **78**, 033014 (2008).

[18] A. Malkus, J. Kneller, G. McLaughlin, and R. Surman, Phys. Rev. D **86**, 085015 (2012).

[19] A. Malkus, A. Friedland, and G. McLaughlin, arXiv:1403.5797.

[20] P. Strack and A. Burrows, Phys. Rev. D **71**, 093004 (2005).

[21] Y. Pehlivan, A. Balantekin, T. Kajino, and T. Yoshida, Phys. Rev. D **84**, 065008 (2011).

[22] J. F. Cherry, J. Carlson, A. Friedland, G. M. Fuller, and A. Vlasenko, Phys. Rev. Lett. **108**, 261104 (2012).

[23] C. Volpe, D. Vnnen, and C. Espinoza, Phys. Rev. D **87**, 113010 (2013).

[24] A. Vlasenko, G. M. Fuller, and V. Cirigliano, Phys. Rev. D **89**, 105004 (2014).

[25] H. Duan and S. Shalgar, Phys. Lett. B **747**, 139 (2015).

[26] E. Pllumbi, I. Tamborra, S. Wanajo, H. T. Janka, and L. Huedepohl, Astrophys. J. **808**, 188 (2015).

[27] A. Mirizzi, G. Mangano, and N. Saviano, Phys. Rev. D **92**, 021702 (2015).

[28] N. F. Bell, R. F. Sawyer, and R. R. Volkas, Phys. Lett. B **500**, 16 (2001).

[29] S. Pastor, G. G. Raffelt, and D. V. Semikoz, Phys. Rev. D **65**, 053011 (2002).

[30] H. Duan, G. M. Fuller, and Y.-Z. Qian, Phys. Rev. D **74**, 123004 (2006).

[31] S. Hannestad, G. G. Raffelt, G. Sigl, and Y. Y. Wong, Phys. Rev. D **74**, 105010 (2006).

[32] H. Duan, G. M. Fuller, J. Carlson, and Y.-Z. Qian, Phys. Rev. D **75**, 125005 (2007).

[33] B. Dasgupta, A. Dighe, A. Mirizzi, and G. G. Raffelt, Phys. Rev. D **77**, 113007 (2008).

[34] H. Duan, G. M. Fuller, J. Carlson, and Y.-Z. Qian, Phys. Rev. Lett. **100**, 021101 (2008).

[35] A. Balantekin and Y. Pehlivan, J. Phys. G **34**, 47 (2007).

[36] A. Esteban-Pretel, S. Pastor, R. Tomàs, G. G. Raffelt, P. D. Serpico, and G. Sigl, Phys. Rev. D **78**, 085012 (2008).

[37] J. Gava, J. Kneller, C. Volpe, and G. McLaughlin, Phys. Rev. Lett. **103**, 071101 (2009).

[38] H. Duan and A. Friedland, Phys. Rev. Lett. **106**, 091101 (2011).

[39] H. Duan, A. Friedland, G. C. McLaughlin, and R. Surman, J. Phys. G **38**, 035201 (2011).

[40] R. Oechslin, H.-T. Janka, and A. Marek, Astron. Astrophys. **467**, 395 (2007).

[41] H.-T. Janka (private communication).

[42] S. Setiawan, M. Ruffert, and H.-T. Janka, arXiv:astro-ph/0509300.

[43] M. Ruffert, H. T. Ruffert, and H.-T. Janka, arXiv:astro-ph/0106229.

[44] H. T. Janka, T. Eberl, M. Ruffert, and C. Fryer, arXiv:astro-ph/9908290.

[45] R. Surman and G. McLaughlin, Astrophys. J. **618**, 397 (2005).

[46] R. F. Sawyer, Phys. Rev. D **79**, 105003 (2009).

[47] K. Olive *et al.* (Particle Data Group Collaboration), Chin. Phys. C **38**, 090001 (2014).

[48] A. Vlasenko, G. M. Fuller, and V. Cirigliano, arXiv:1406.6724.

[49] C. Horowitz, Phys. Rev. D **65**, 043001 (2002).

[50] G. M. Fuller and B. S. Meyer, Astrophys. J. **453**, 792 (1995).

[51] B. S. Meyer, G. C. McLaughlin, and G. M. Fuller, Phys. Rev. C **58**, 3696 (1998).

[52] B. D. Metzger, T. A. Thompson, and E. Quataert, Astrophys. J. **676**, 1130 (2008).

[53] O. L. Caballero, G. C. McLaughlin, and R. Surman, Astrophys. J. **745**, 170 (2012).